Supporting Information

Enhanced Electrocatalytic Hydrogen Evolution with Bimetallic Ru/Pt Nanoparticles Supported on Nitrogen-Doped Reduced Graphene Oxide

Heting Hou[a,b] §, Christian Cerezo-Navarrete[c] §, Dídac A. Fenoll[d], Matilda Kraft[b], Carlo Marini[e], Luis Rodríguez-Santiago[d], Xavier Solans-Monfort[d]*, Luis M. Martínez-Prieto[c, f]*, Nuria Romero[b,g]*, Jordi García-Antón[b]*, Xavier Sala[b]

a School of Chemical and Environmental Engineering, Liaoning University of Technology, Jinzhou, 121001, Liaoning Province, P. R. China

b Departament de Química, Unitat de Química Inorgànica, Universitat Autònoma de Barcelona, 08193 Cerdanyola del Vallès (Barcelona), Spain

c ITQ, Instituto de Tecnología Química, Universitat Politècnica de València (UPV), Av. de los Naranjos S/N, 46022, Valencia, Spain.

d Departament de Química, Unitat de Química Física, Universitat Autònoma de Barcelona, 08193 Cerdanyola del Vallès (Barcelona), Spain

e ALBA Synchrotron Light Facility, Carrer de la Llum 2-26, 08290, Cerdanyola del Valles, Barcelona, Spain

f IIQ, Instituto de Investigaciones Químicas (CSIC-Universidad de Sevilla), Avda. Americo Vespucio 49, 41092, Seville, Spain.

g CNRS, LCC (Laboratoire de Chimie de Coordination), UPR8241, University of Toulouse, UPS, INPT, Toulouse cedex 4 F-31077, France.

§ Joint first authors with equal contributions

Table of contents

Figure S13. Linear sweep voltammetry of **Pt_1Ru_5@NH_2-rGO** upon applying chronopotentiometry at -300 mA·cm^{-2} in 1M H_2SO_4 after 7 h and 19 h. Right: magnified view of the left graph.

Figure S14. Chronoamperometry experiment on Pt_1Ru_5@NH_2-rGO in 1M H_2SO_4 at -300 mA·cm^{-2} over 12 h.

Figure S15. Linear sweep voltammetry of **Pt@NH_2-rGO**, **Pt_5Ru_1@NH_2-rGO**, **Pt_1Ru_1@NH_2-rGO, Pt_1Ru_5@NH_2-rGO** and **Ru@NH_2-rGO** in 1M NaOH at final state. Right: magnified view of the left graph.

Figure S16. Tafel Plot Analysis of **Pt@NH_2-rGO**, **Pt_5Ru_1@NH_2-rGO**, **Pt_1Ru_1@NH_2-rGO, Pt_1Ru_5@NH_2-rGO** and **Ru@NH_2-rGO** in 1M NaOH after stabilization at final state.

Figure S17. ECSA calculation of **Ru@NH_2-rGO** in 1M NaOH at the beginning of the catalysis (top) and at the final state (bottom).

Figure S18. ECSA calculation of **Pt_1Ru_5@NH_2-rGO** in 1M NaOH at the beginning of the catalysis (top) and at the final state (bottom).

Figure S19. ECSA calculation of **Pt_1Ru_1@NH_2-rGO** in 1M NaOH at the beginning of the catalysis (top) and at the final state (bottom).

Figure S20. ECSA calculation of **Pt_5Ru_1@NH_2-rGO** in 1M NaOH at the beginning of the catalysis (top) and at the final state (bottom).

Figure S21. ECSA calculation of **Pt@NH_2-rGO** in 1M NaOH at the beginning of the catalysis (top) and at the final state (bottom).

Figure S22. Optimized structures of all adsorption sites considered for the addition of one H atom to $Pt_{79}H_{105}$.

Figure S23. Optimized structures of all adsorption sites considered for the addition of one H atom to $Ru_{57}H_{61}$.

Figure S24. Optimized structures of all adsorption sites considered for the addition of one H atom to $Pt_{10}Ru_{47}H_{64}$.

Figure S25. Hydrogen evolution reaction mechanisms taking place on the Pt-Ru interface of bimetallic nanoparticles.

Table S1. Computed adsorption energies in kJ mol^{-1} of additional H atoms on the $Pt_{79}H_{105}$, $Ru_{57}H_{61}$ and $Pt_{10}Ru_{47}H_{64}$ nanoparticles.

Table S2. Mean computed adsorption energies (kJ mol^{-1}) of the H monolayer formation ($Ru_{57}H_{44}$ and $Pt_{79}H_{60}$) as well as the mean adsorption energy of the subsequent additional H atoms.

Table S3. Comparison of the most relevant graphene-derived and Pt and/or Ru graphene-based HER nanoelectrocatalysts under acidic conditions. Parameters: mean diameter (Ø), onset overpotential (η_0, mV), overpotential at |j| =10 mA/cm^2 (η_{10}, mV), Tafel slope (b, mV/dec), and exchange current density ($|j_0|$, mA/cm^2). Unless otherwise stated, electrolyte is 0.5 M H_2SO_4.

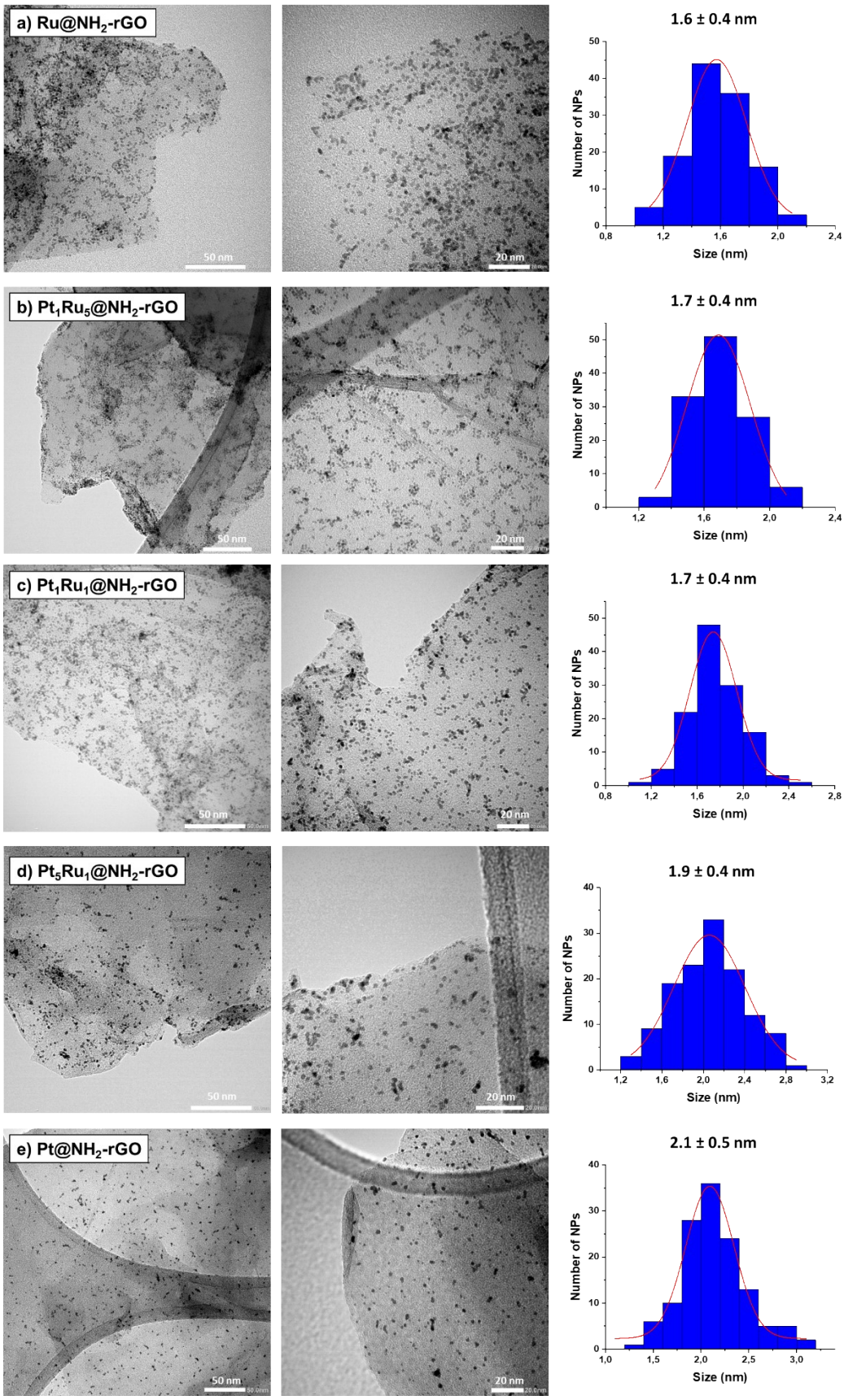

Figure S1. TEM micrographs and the corresponding size histograms of (a) **Ru@NH_2-rGO**, (b) **Pt_1Ru_5@NH_2-rGO**, (c) **Pt_1Ru_1@NH_2-rGO**, (d) **Pt_5Ru_1@NH_2-rGO** , (e) **Pt@NH_2-rGO**.

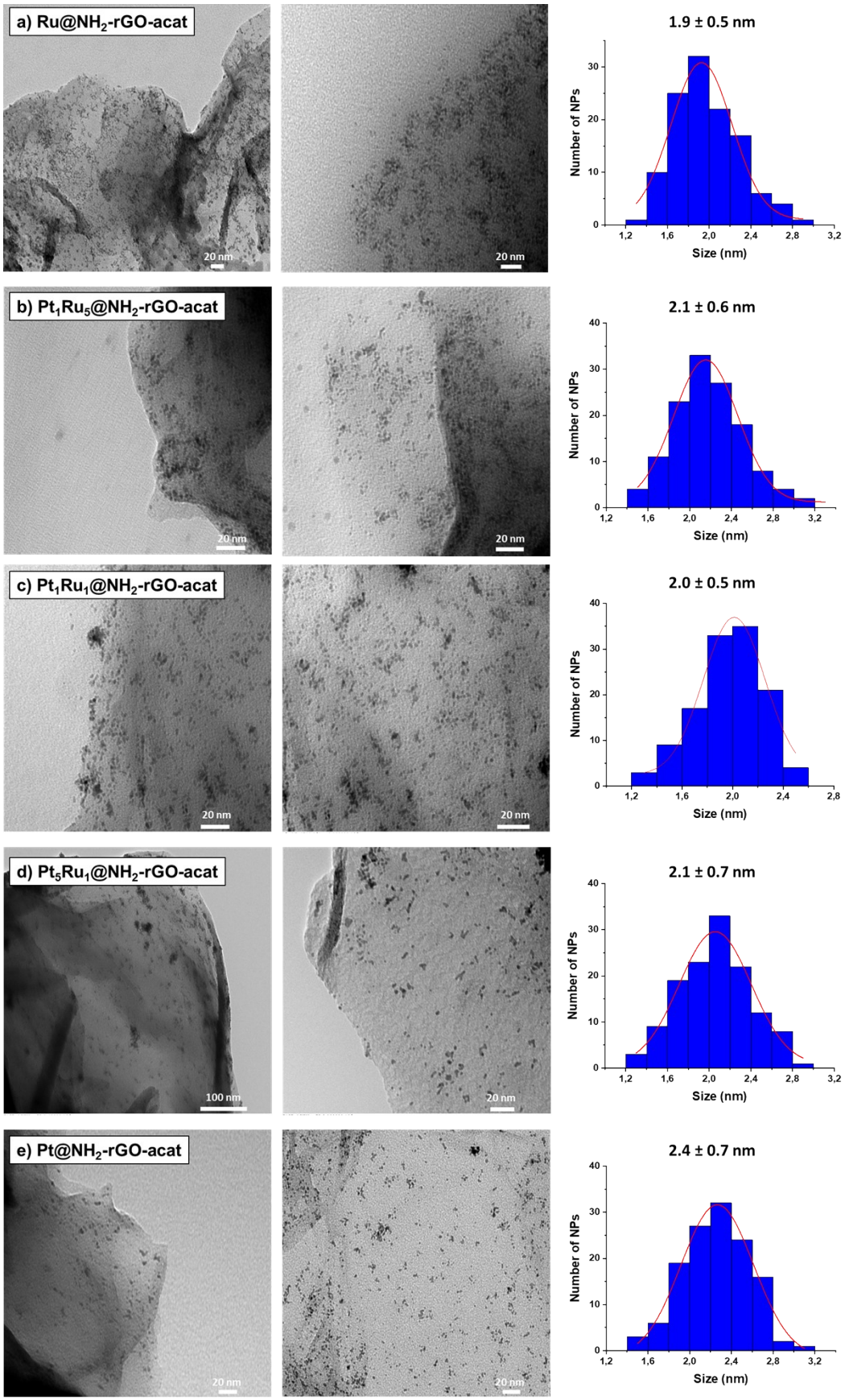

Figure S2. TEM micrographs and the corresponding size histograms of (a) **Ru@NH_2-rGO**, (b) **Pt_1Ru_5@NH_2-rGO**, (c) **Pt_1Ru_1@NH_2-rGO**, (d) **Pt_5Ru_1@NH_2-rGO**, (e) **Pt@NH_2-rGO** after catalysis.

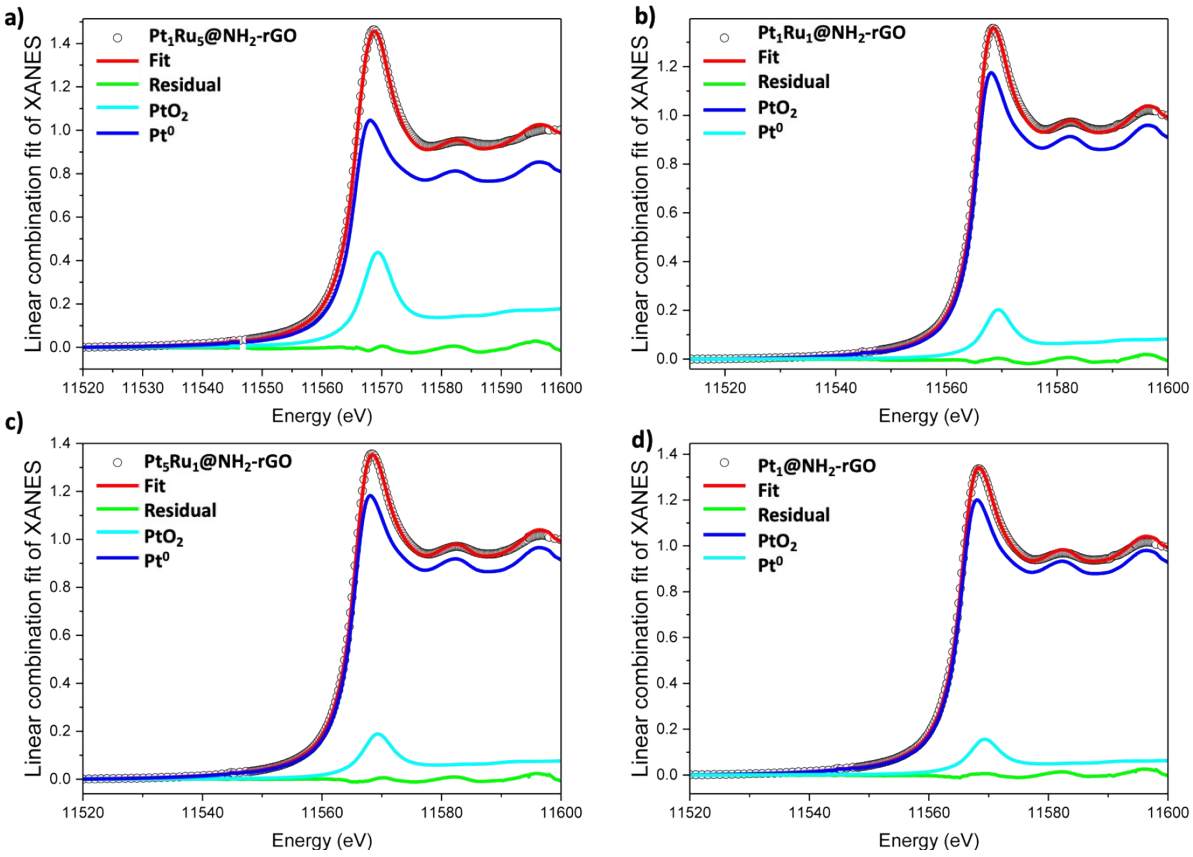

Figure S3. Linear combination fitting of XANES spectra of a) **Pt_1Ru_5@NH_2-rGO**, b) **Pt_1Ru_1@NH_2-rGO,** c) **Pt_5Ru_1@NH_2-rGO** and d) **Pt@NH_2-rGO** at Pt L3 edge.

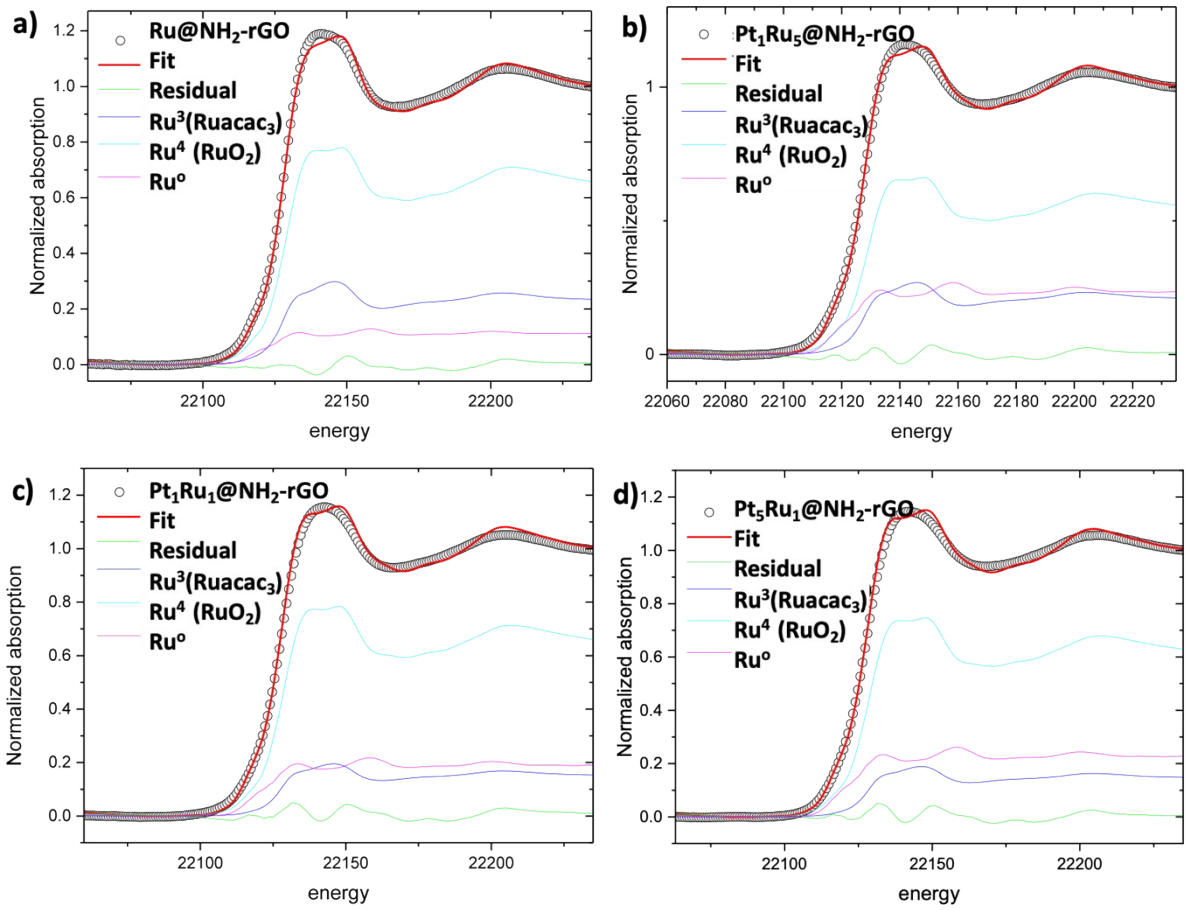

Figure S4. Linear combination fitting of XANES spectra of a) **Ru@NH$_2$-rGO**, b) **Pt$_1$Ru$_5$@NH$_2$-rGO**, c) **Pt$_1$Ru$_1$@NH$_2$-rGO** and d) **Pt$_5$Ru$_1$@NH$_2$-rGO** at Ru K edge.

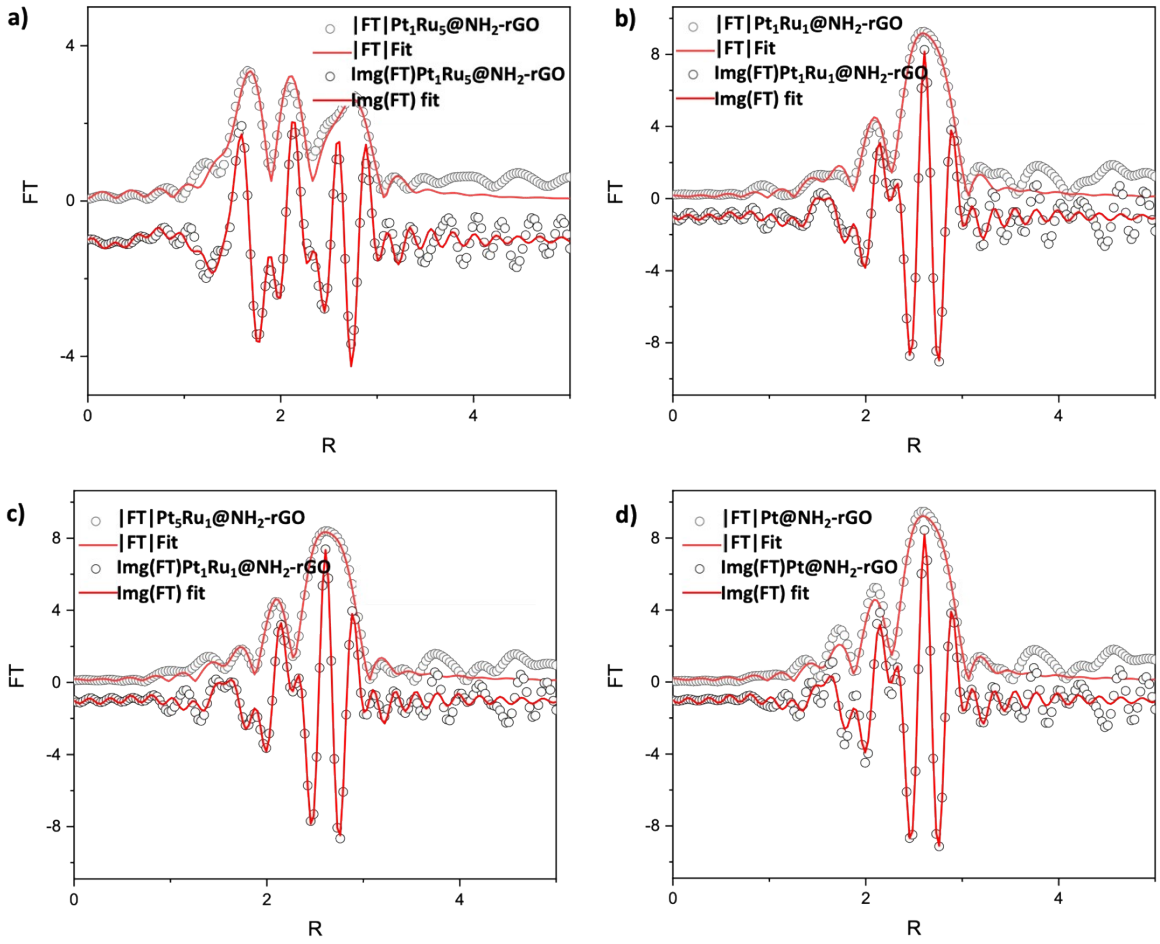

Figure S5. EXAFS spectra and Fourier Transform of a) **Pt_1Ru_5@NH_2-rGO**, b) **Pt_1Ru_1@NH_2-rGO**, c) **Pt_5Ru_1@NH_2-rGO** and d) **Pt@NH_2-rGO** at Pt L3 edge.

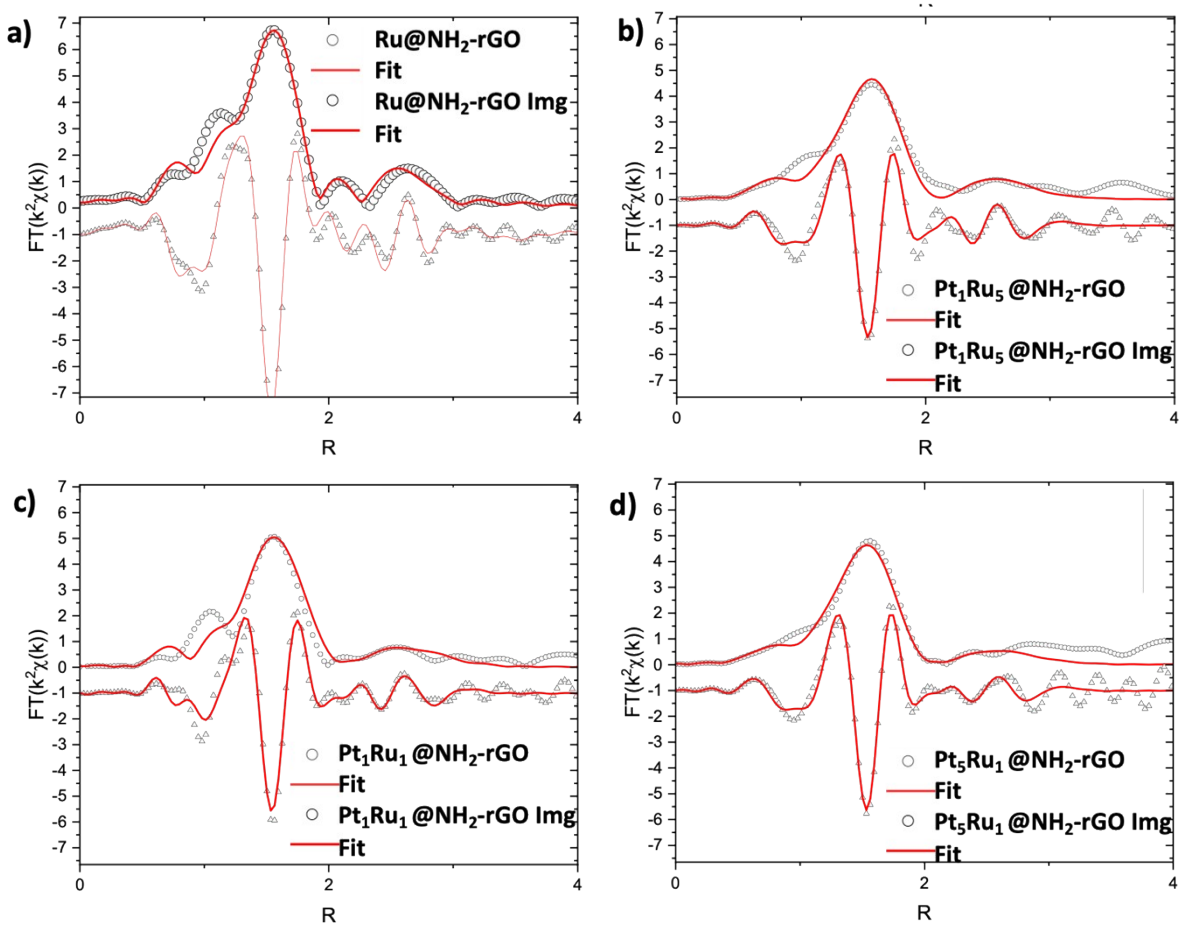

Figure S6. EXAFS spectra and Fourier Transform of a) **Ru@NH_2-rGO**, b) **Pt_1Ru_5@NH_2-rGO**, c) **Pt_1Ru_1@NH_2-rGO** and d) **Pt_5Ru_1@NH_2-rGO** at Ru K edge.

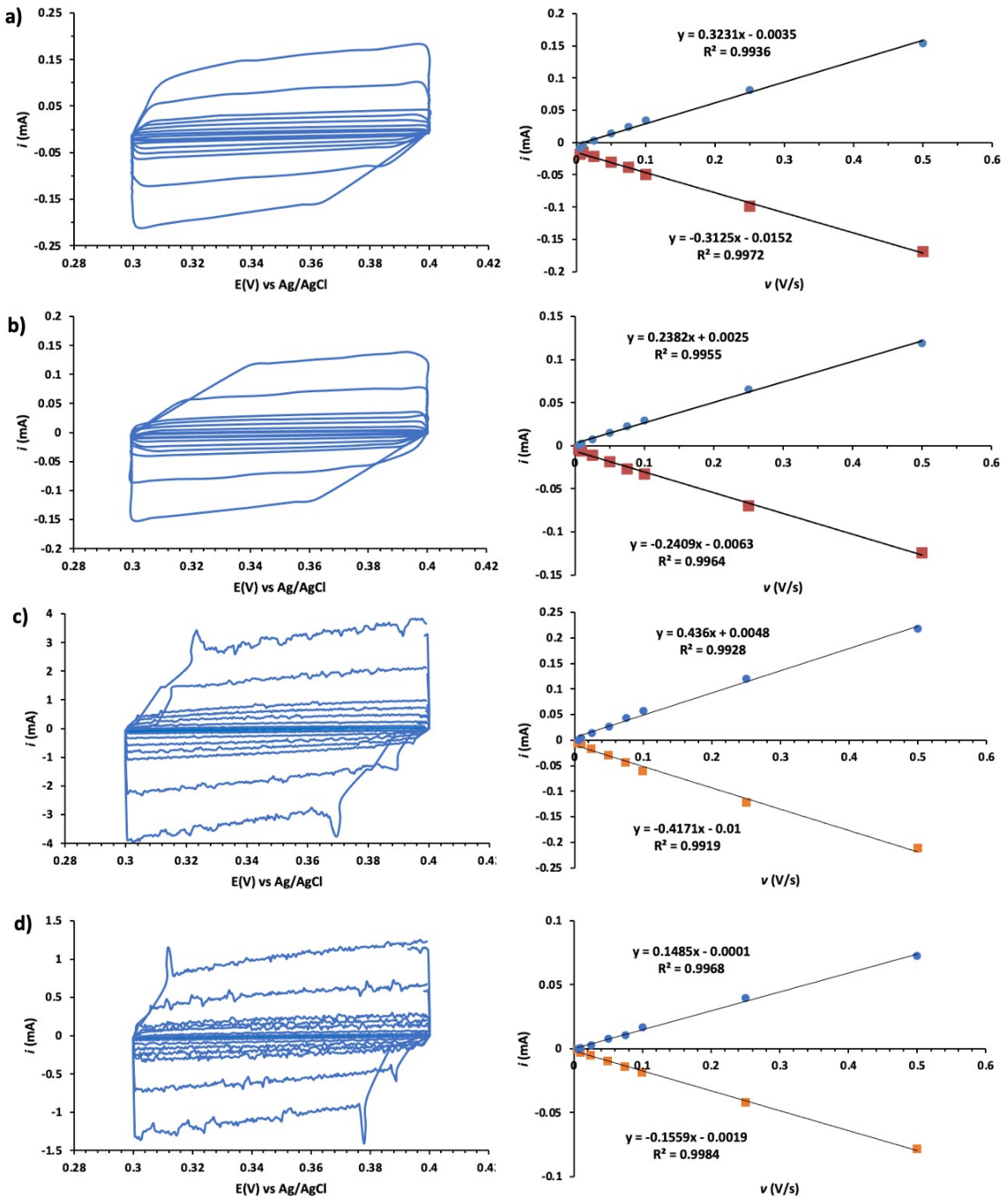
a)
i (mA)
E(V) vs Ag/AgCl
y = 0.3231x - 0.0035
R² = 0.9936
y = -0.3125x - 0.0152
R² = 0.9972
v (V/s)
b)
i (mA)
E(V) vs Ag/AgCl
y = 0.2382x + 0.0025
R² = 0.9955
y = -0.2409x - 0.0063
R² = 0.9964
v (V/s)
c)
i (mA)
E(V) vs Ag/AgCl
y = 0.436x + 0.0048
R² = 0.9928
y = -0.4171x - 0.01
R² = 0.9919
v (V/s)
d)
i (mA)
E(V) vs Ag/AgCl
y = 0.1485x - 0.0001
R² = 0.9968
y = -0.1559x - 0.0019
R² = 0.9984
v (V/s)

e)

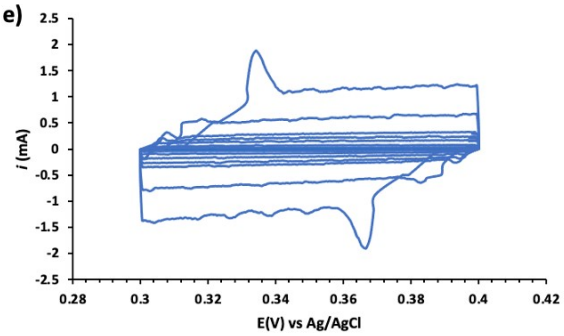
i (mA)
E(V) vs Ag/AgCl

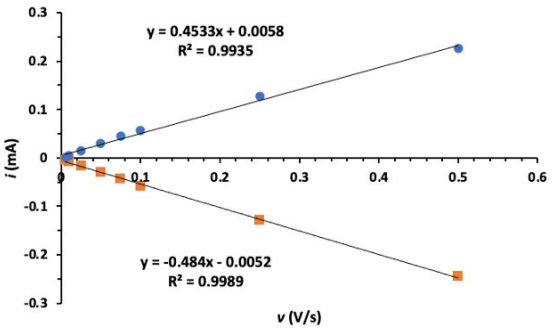
y = 0.4533x + 0.0058
R² = 0.9935
y = -0.484x - 0.0052
R² = 0.9989
i (mA)
v (V/s)

f)

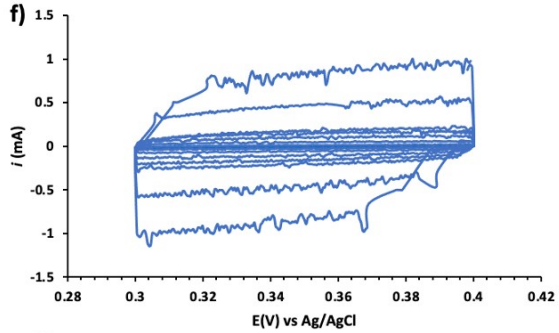
i (mA)
E(V) vs Ag/AgCl

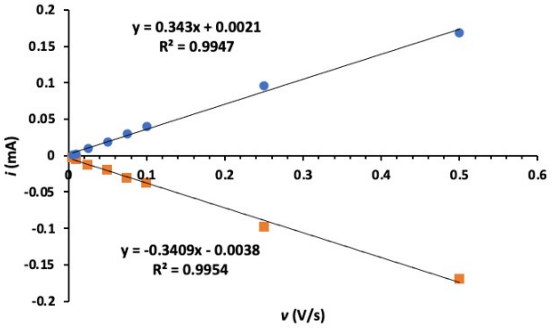
y = 0.343x + 0.0021
R² = 0.9947
y = -0.3409x - 0.0038
R² = 0.9954
i (mA)
v (V/s)

g)

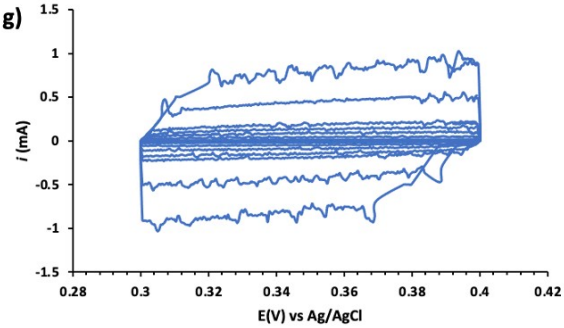
i (mA)
E(V) vs Ag/AgCl

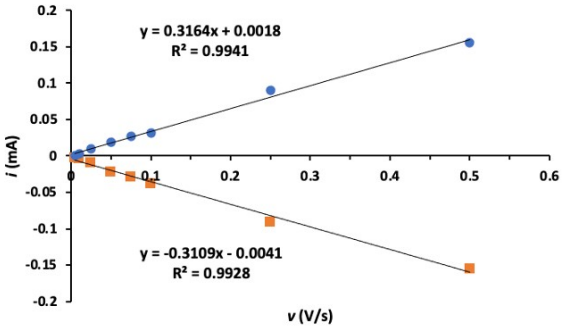
y = 0.3164x + 0.0018
R² = 0.9941
y = -0.3109x - 0.0041
R² = 0.9928
i (mA)
v (V/s)

h)

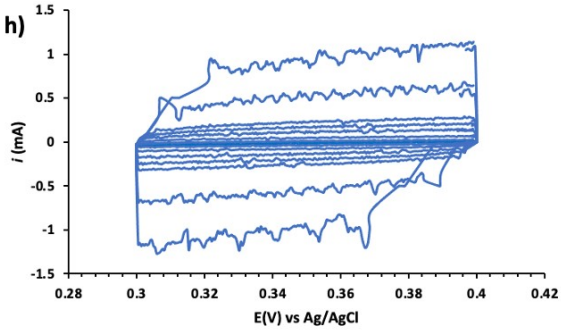
i (mA)
E(V) vs Ag/AgCl

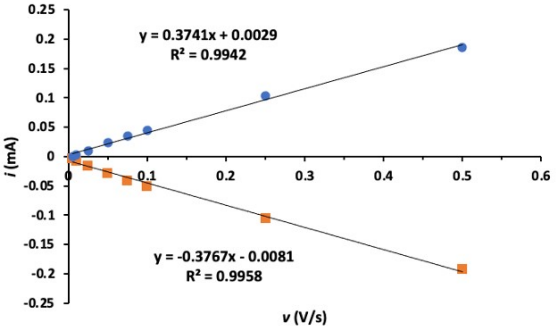
y = 0.3741x + 0.0029
R² = 0.9942
y = -0.3767x - 0.0081
R² = 0.9958
i (mA)
v (V/s)

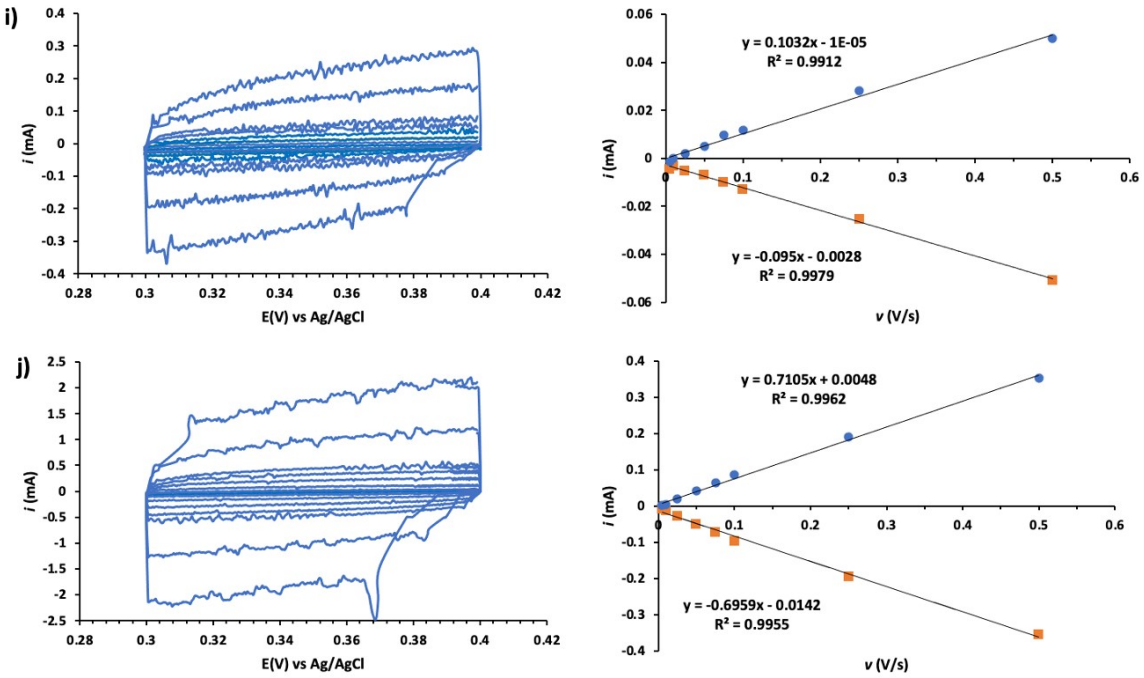

Figure S7. Multi CV experiment at different scan rates for C_{DL} determination (left) and plot of current values at 0.35 V (vs. Ag/AgCl) for the different scan rates (right) of **Pt@NH$_2$-rGO** before (a) and after (b) reductive potential; **Pt$_5$Ru$_1$@NH$_2$-rGO** before (c) and after (d) reductive potential; **Pt$_1$Ru$_1$@NH$_2$-rGO** before(e) and after(f) reductive potential; **Pt$_1$Ru$_5$@NH$_2$-rGO** before (g) and after (h) reductive potential and **Ru@NH$_2$-rGO** before (i) and after (j) reductive potential in 1 M H_2SO_4.

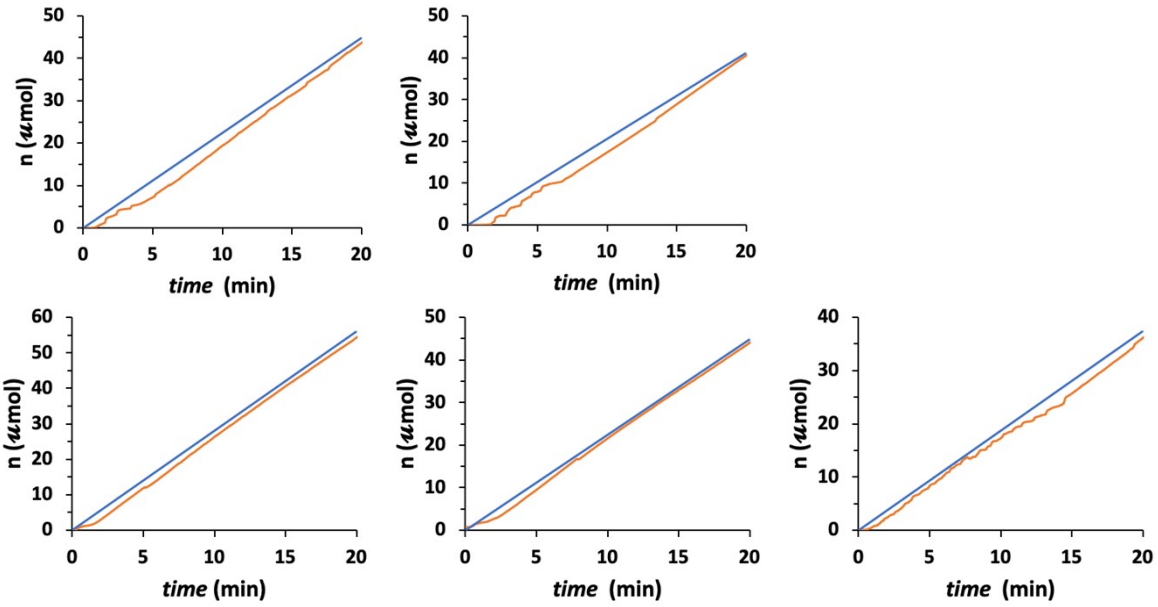

Figure S8. H_2-monitored (solid orange) current-controlled bulk electrolysis (solid blue) of a) **Pt@NH$_2$-rGO**, b) **Pt$_5$Ru$_1$@NH$_2$-rGO**, c) **Pt$_1$Ru$_1$@NH$_2$-rGO**, d) **Pt$_1$Ru$_5$@NH$_2$-rGO**, and e) **Ru@NH$_2$-rGO** in 1 M H_2SO_4. The production of H_2 was detected in the gas phase by using a Clark-type electrode.

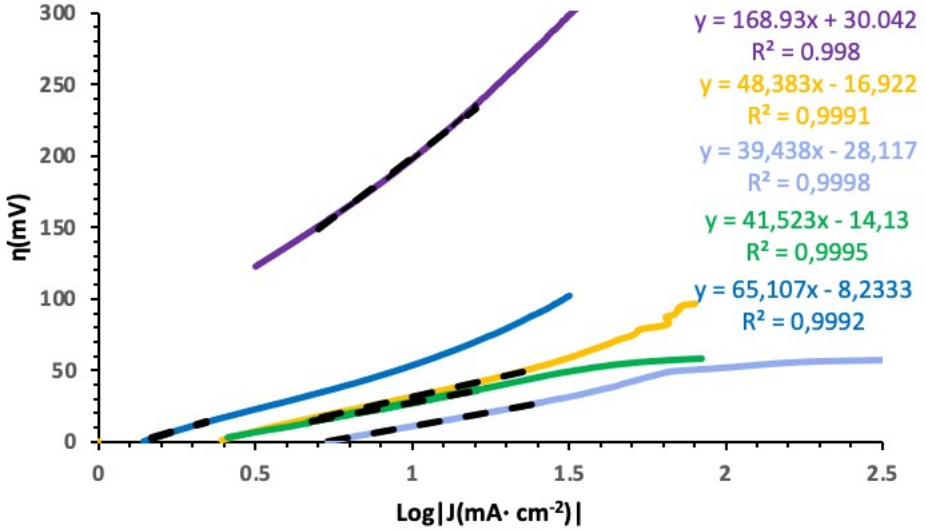

Figure S9. Tafel plots of all materials studied in this work as-synthesized deposited on RDE in acidic conditions. **Pt@NH$_2$-rGO** (pastel blue), **Pt$_5$Ru$_1$@NH$_2$-rGO** (yellow), **Pt$_1$Ru$_1$@NH$_2$-rGO** (green), **Pt$_1$Ru$_5$@NH$_2$-rGO** (blue) and **Ru@NH$_2$-rGO** (purple).

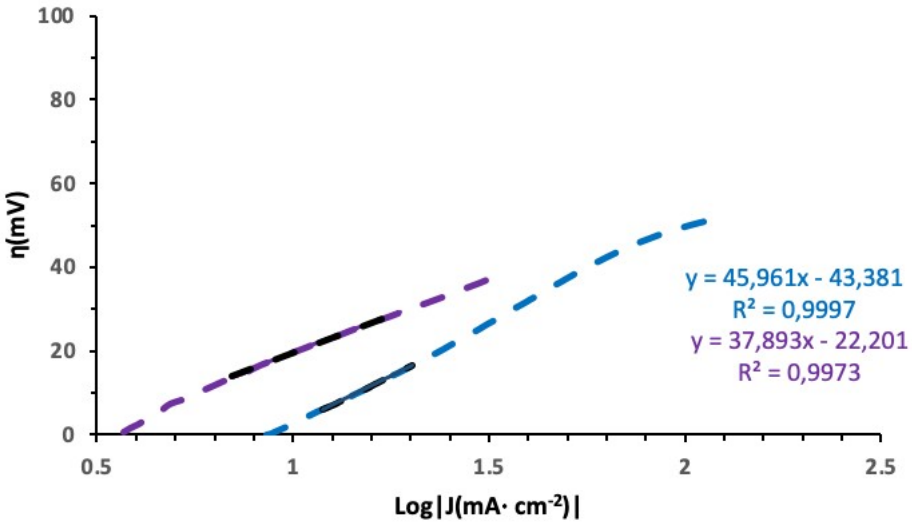

Figure S10. Tafel plots of **Ru@NH$_2$-rGO** (purple) and **Pt$_1$Ru$_5$@NH$_2$-rGO** (blue) after full activation under reductive conditions (j = -10 mA/cm^2).

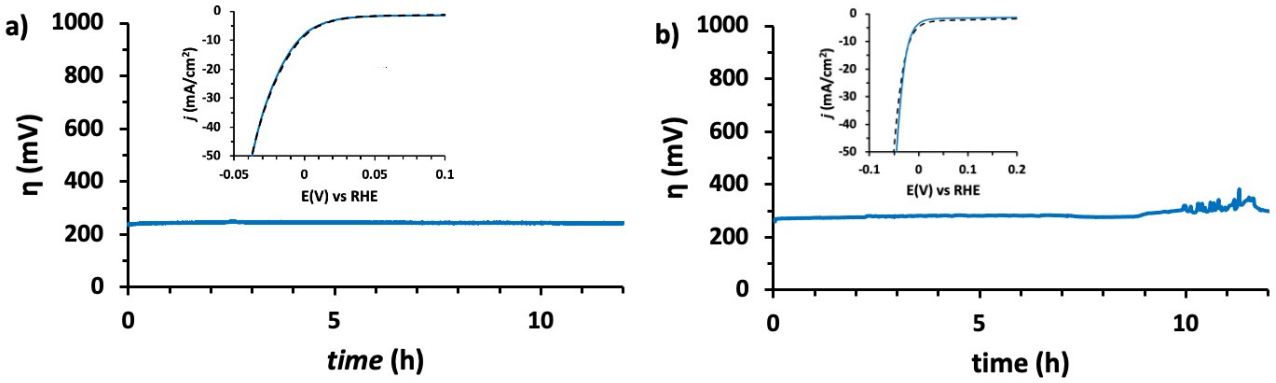

Figure S11. 12 hours bulk electrolysis of a) **Ru$_5$Pt$_1$@NH$_2$-rGO** and b) **Ru@NH$_2$-rGO** at j = -10 mA/cm^2 in 1 M H_2SO_4 solution. Inset: polarization curves before (bold blue) and after (dashed black) 12 h bulk electrolysis.

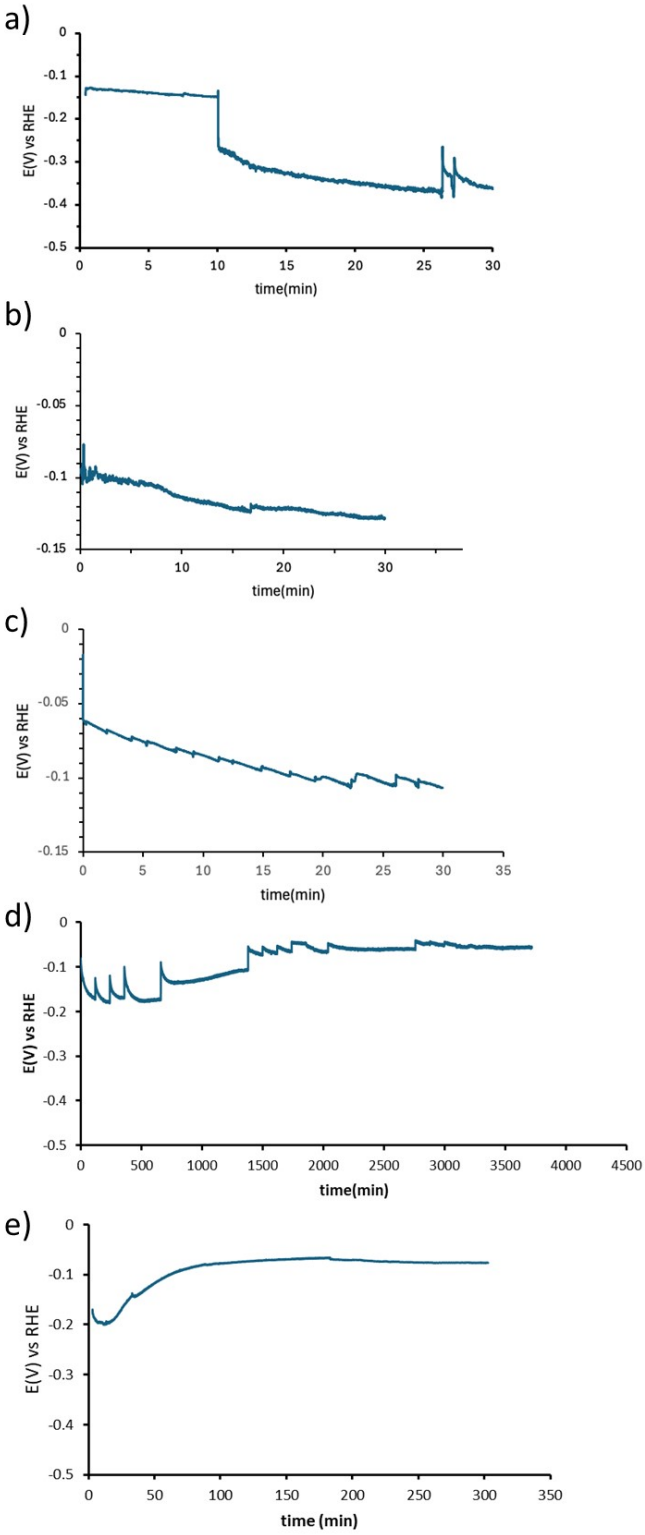

Figure S12. Chronopotentiommetry experiments of all as-synthetized materials at at j = -10 mA/cm^2 in 1 M H_2SO_4 solution. a) **Pt@NH$_2$-rGO**, b) **Pt$_5$Ru$_1$@NH$_2$-rGO**, c) **Pt$_1$Ru$_1$@NH$_2$-rGO**, d) **Pt$_1$Ru$_5$@NH$_2$-rGO**, and e) **Ru@NH$_2$-rGO.**

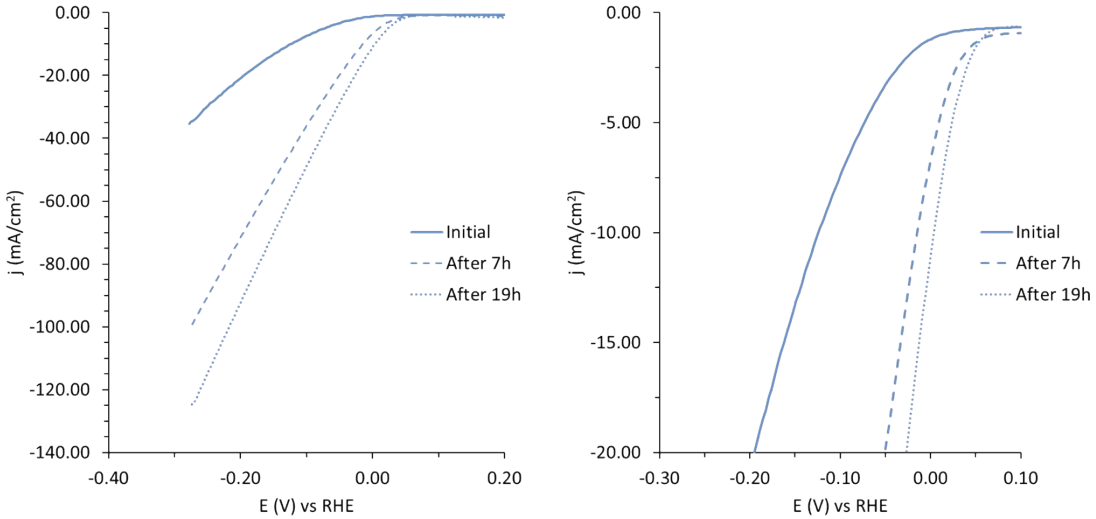

Figure S13. Linear sweep voltammetry of **Pt_1Ru_5@NH_2-rGO** upon applying chronopotentiometry at -300 mA·cm^{-2} in 1M H_2SO_4 after 7 h and 19 h. Right: magnified view of the left graph.

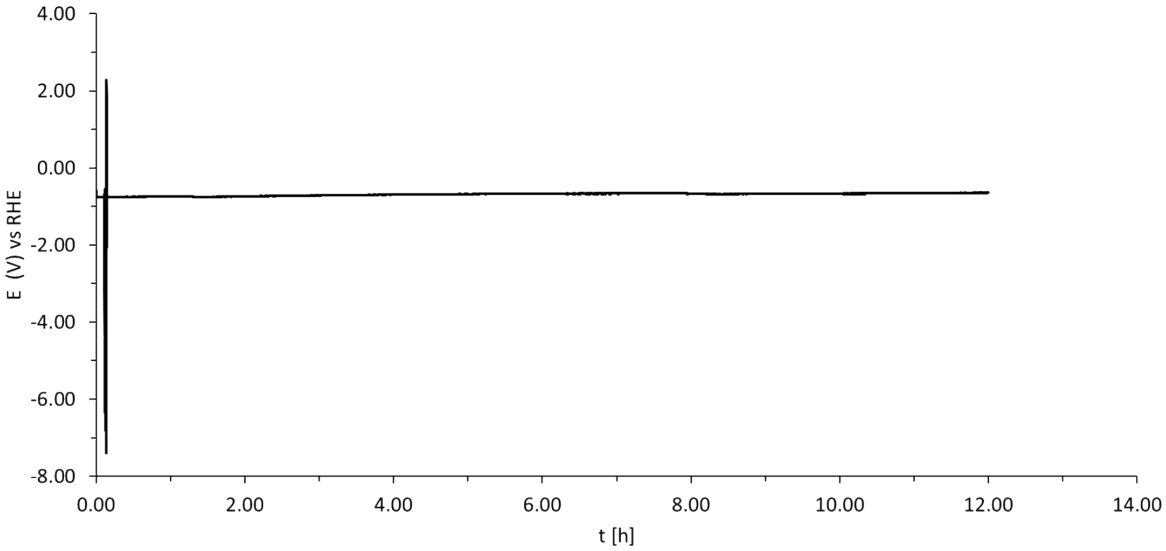

Figure S14. Chronoamperometry experiment on Pt_1Ru_5@NH_2-rGO in 1M H_2SO_4 at -300 mA·cm^{-2} over 12 h.

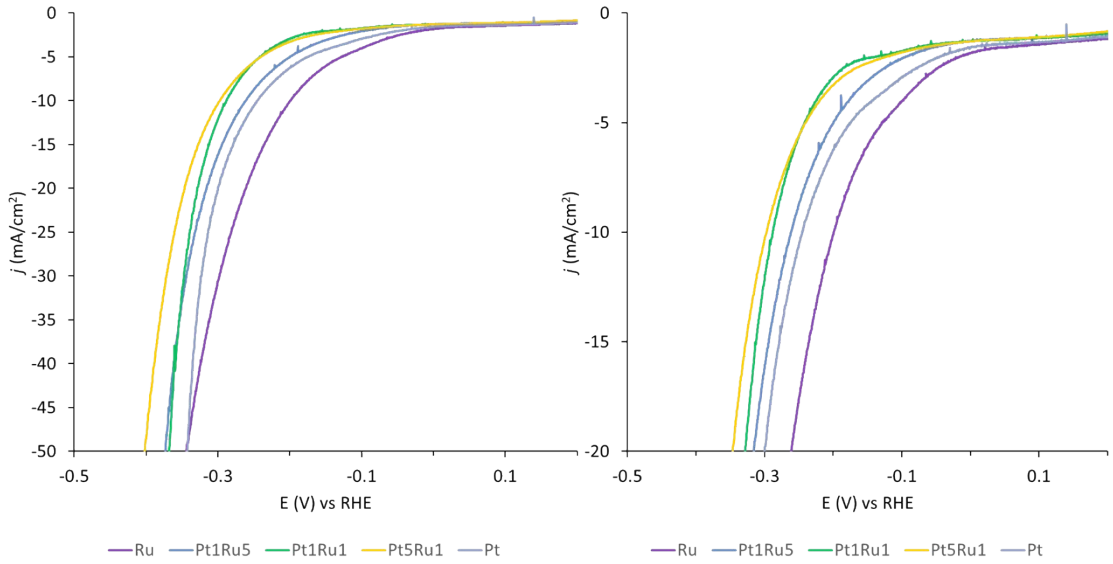

Figure S15. Linear sweep voltammetry of **Pt@NH_2-rGO**, **Pt_5Ru_1@NH_2-rGO**, **Pt_1Ru_1@NH_2-rGO, Pt_1Ru_5@NH_2-rGO** and **Ru@NH_2-rGO** in 1M NaOH at final state. Right: magnified view of the left graph.

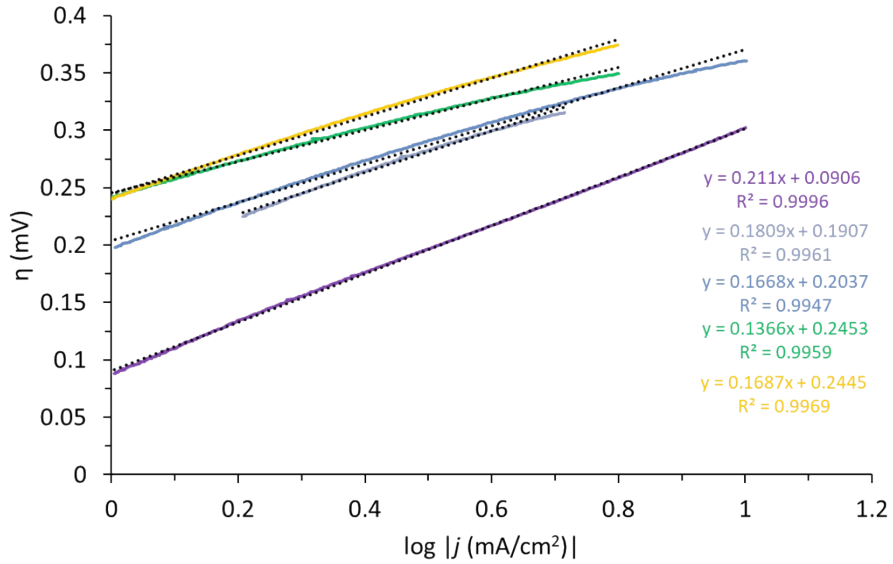

Figure S16. Tafel Plot Analysis of **Pt@NH_2-rGO**, **Pt_5Ru_1@NH_2-rGO**, **Pt_1Ru_1@NH_2-rGO, Pt_1Ru_5@NH_2-rGO** and **Ru@NH_2-rGO** in 1M NaOH after stabilization at final state.

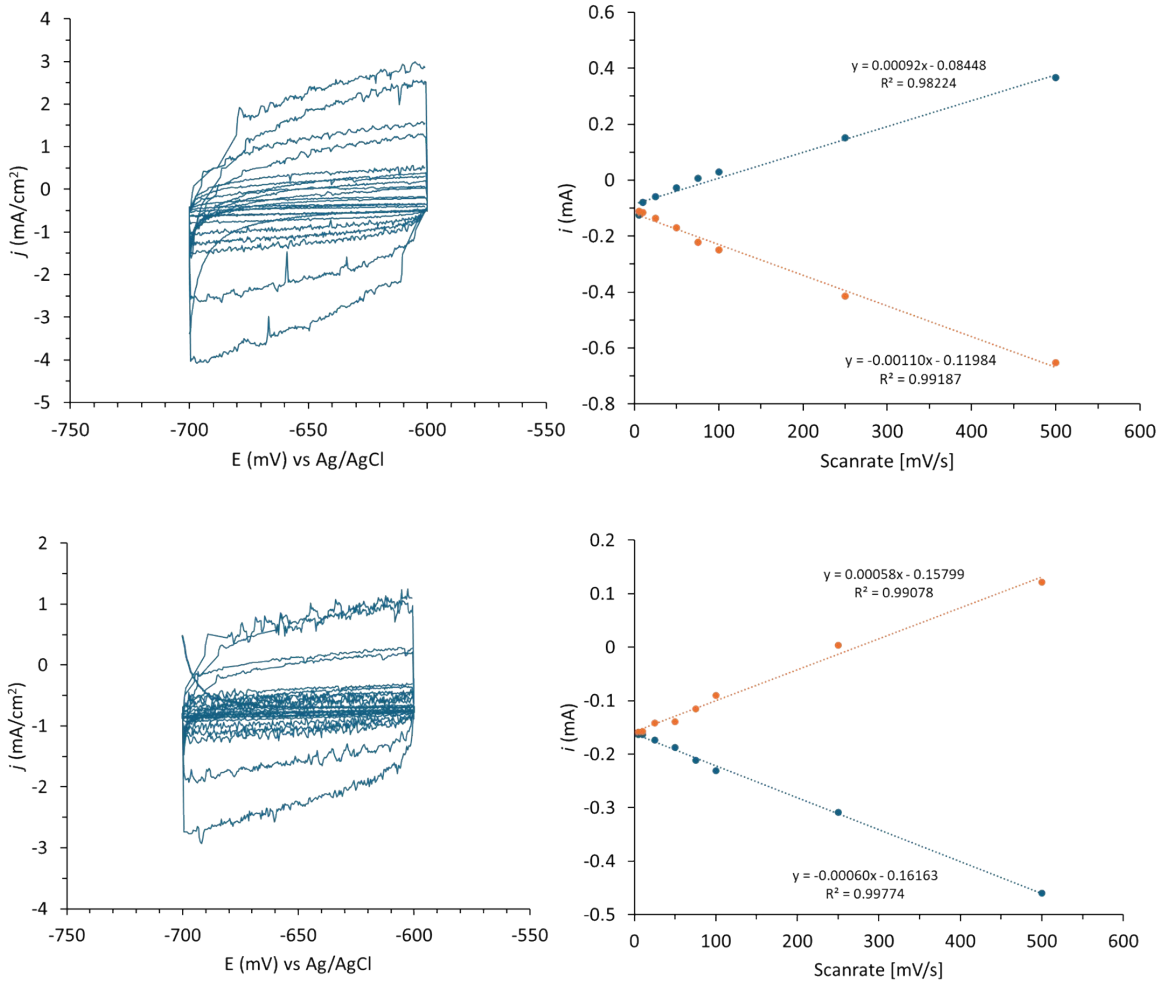

Figure S17. ECSA calculation of **Ru@NH_2-rGO** in 1M NaOH at the beginning of the catalysis (top) and at the final state (bottom).

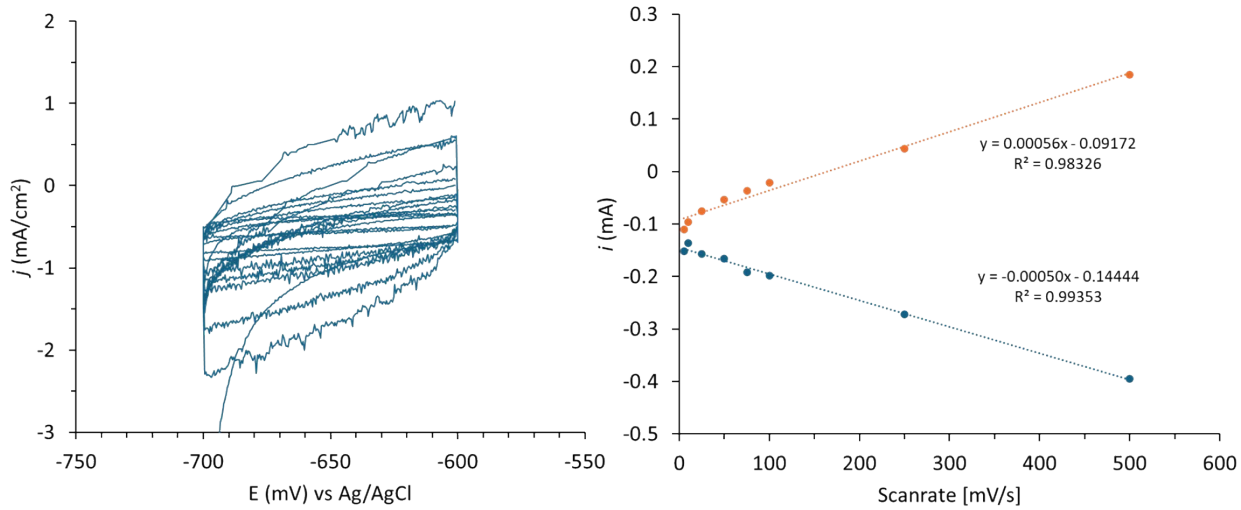

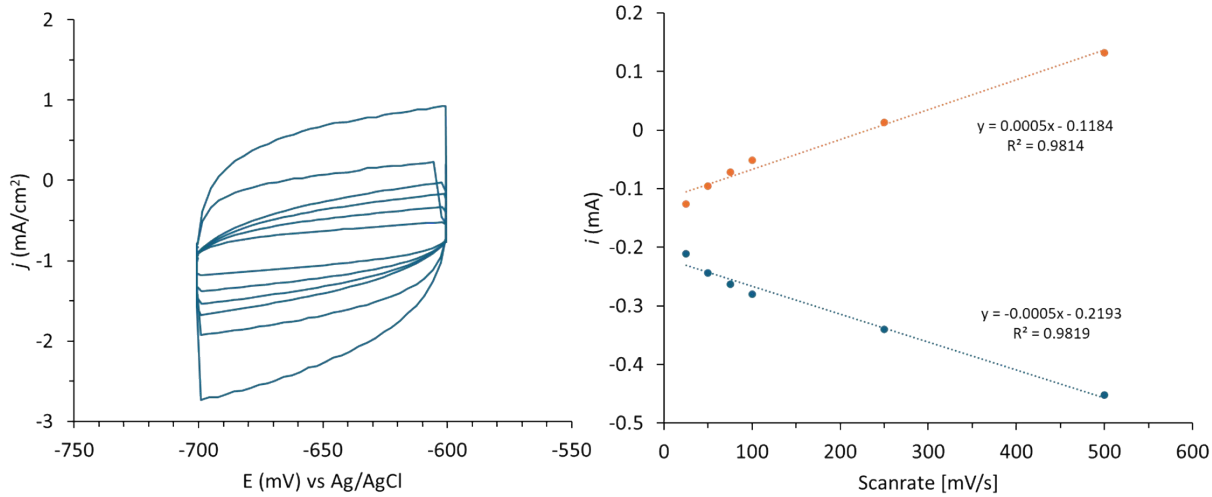

Figure S18. ECSA calculation of **Pt_1Ru_5@NH_2-rGO** in 1M NaOH at the beginning of the catalysis (top) and at the final state (bottom).

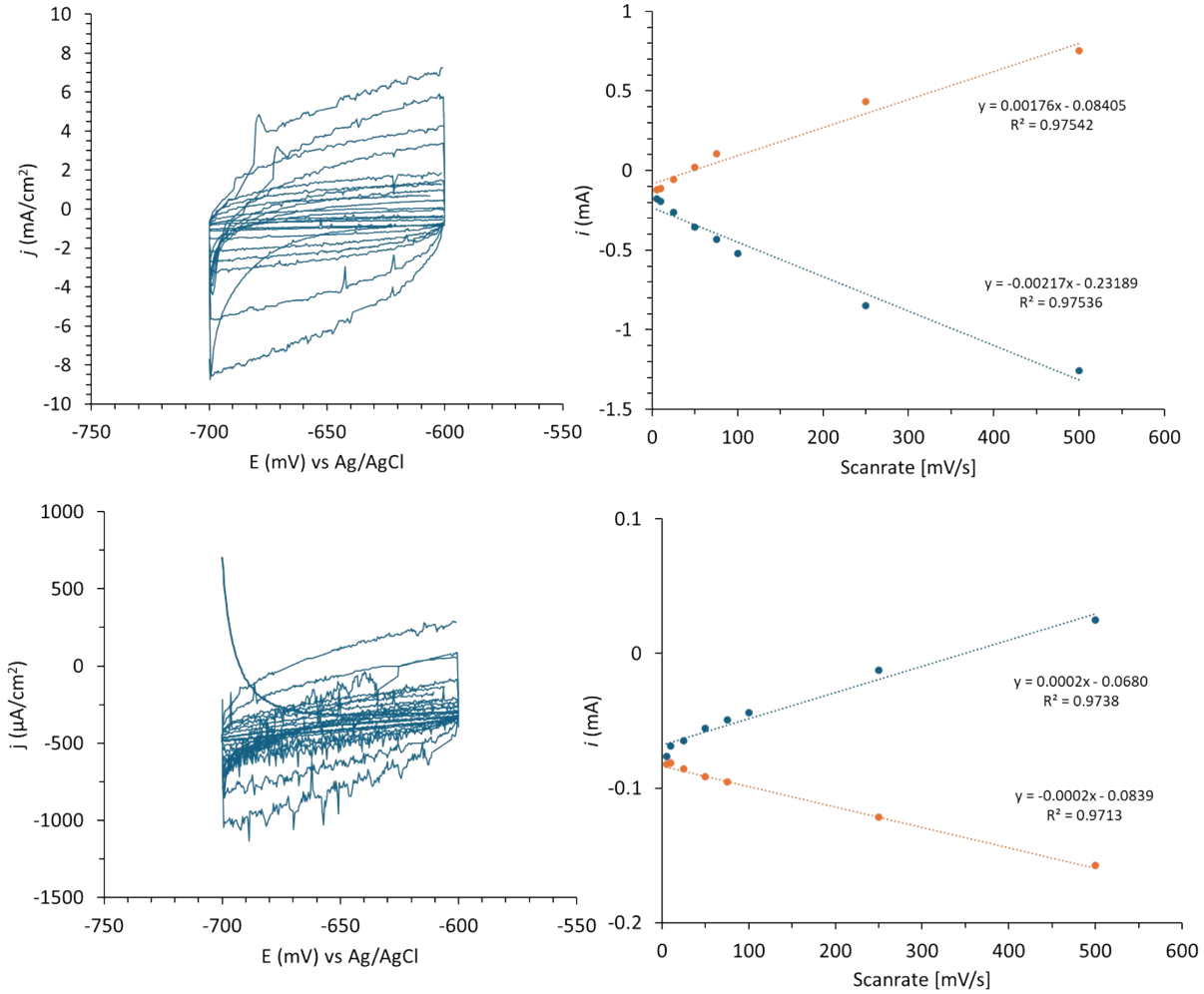

Figure S19. ECSA calculation of **Pt_1Ru_1@NH_2-rGO** in 1M NaOH at the beginning of the catalysis (top) and at the final state (bottom).

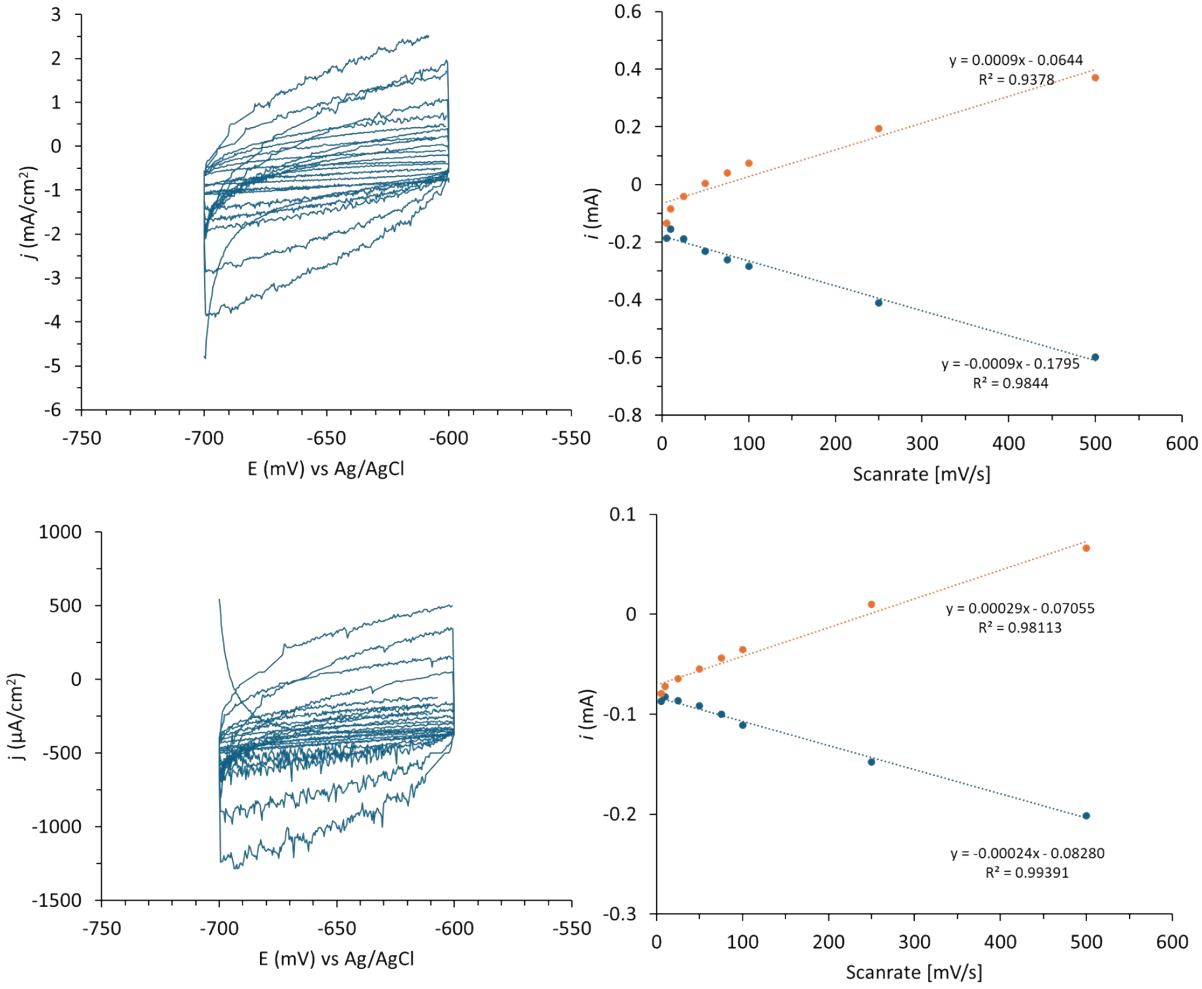

Figure S20. ECSA calculation of **Pt_5Ru_1@NH_2-rGO** in 1M NaOH at the beginning of the catalysis (top) and at the final state (bottom).

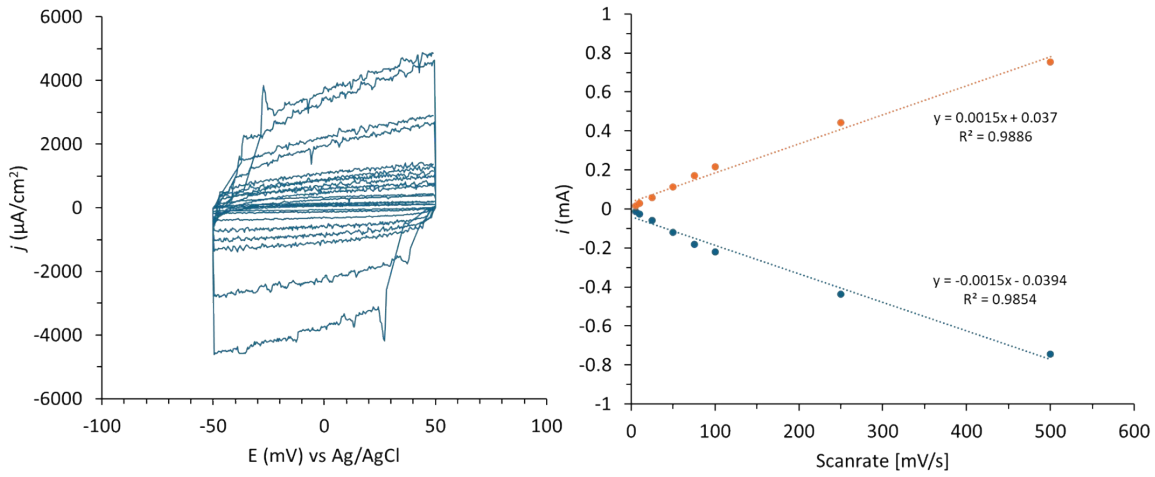

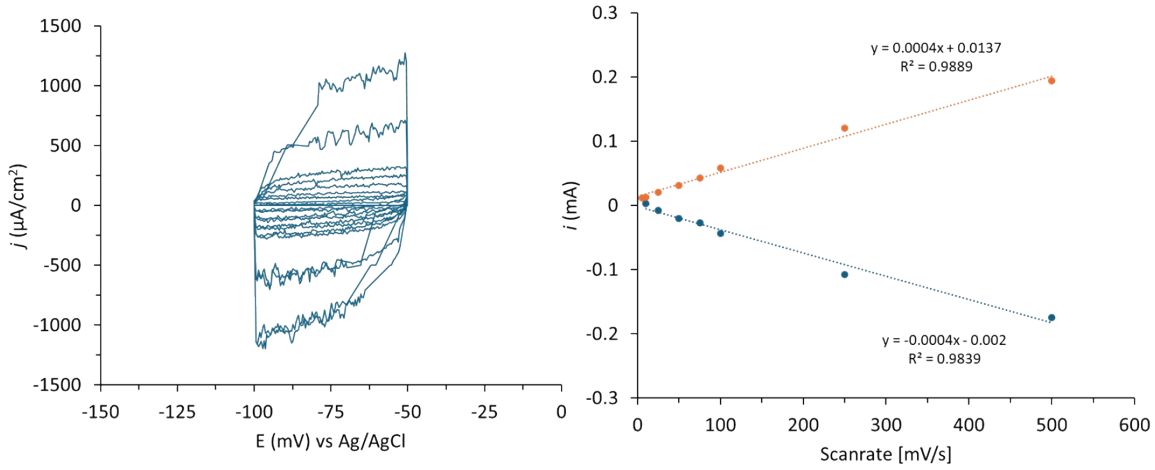

Figure S21. ECSA calculation of **Pt@NH_2-rGO** in 1M NaOH at the beginning of the catalysis (top) and at the final state (bottom).

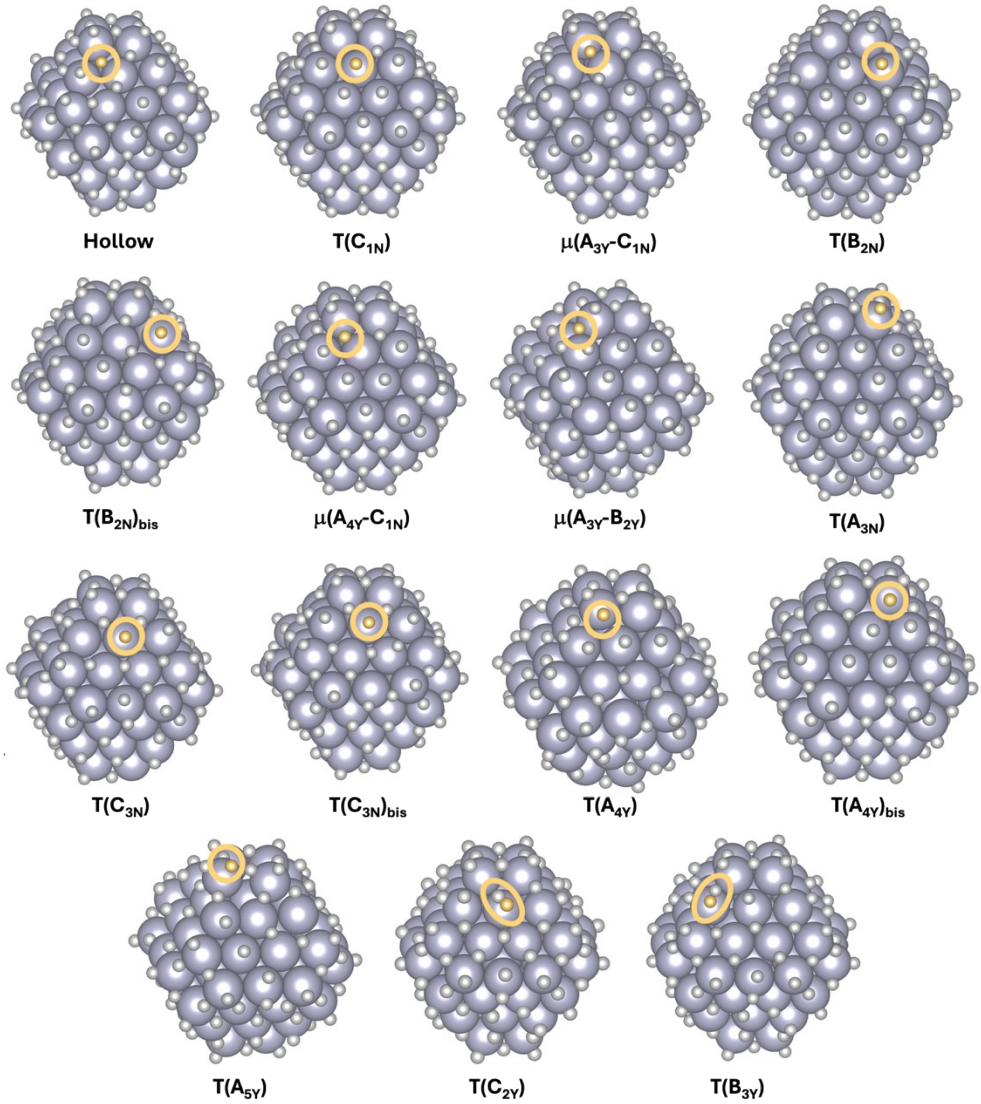

Figure S22. Optimized structures of all adsorption sites considered for the addition of one H atom to $Pt_{79}H_{105}$.

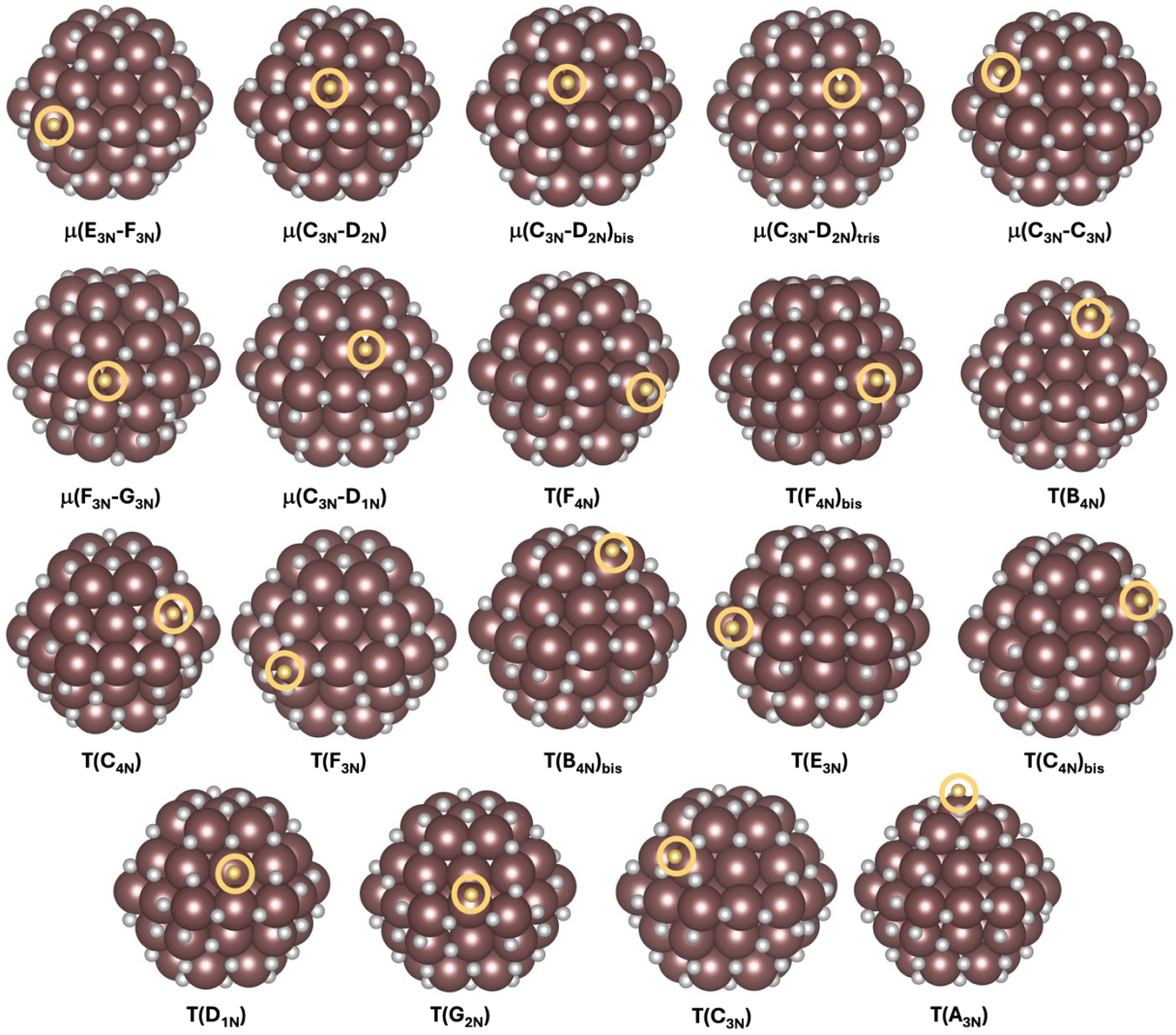

Figure S23. Optimized structures of all adsorption sites considered for the addition of one H atom to $Ru_{57}H_{61}$.

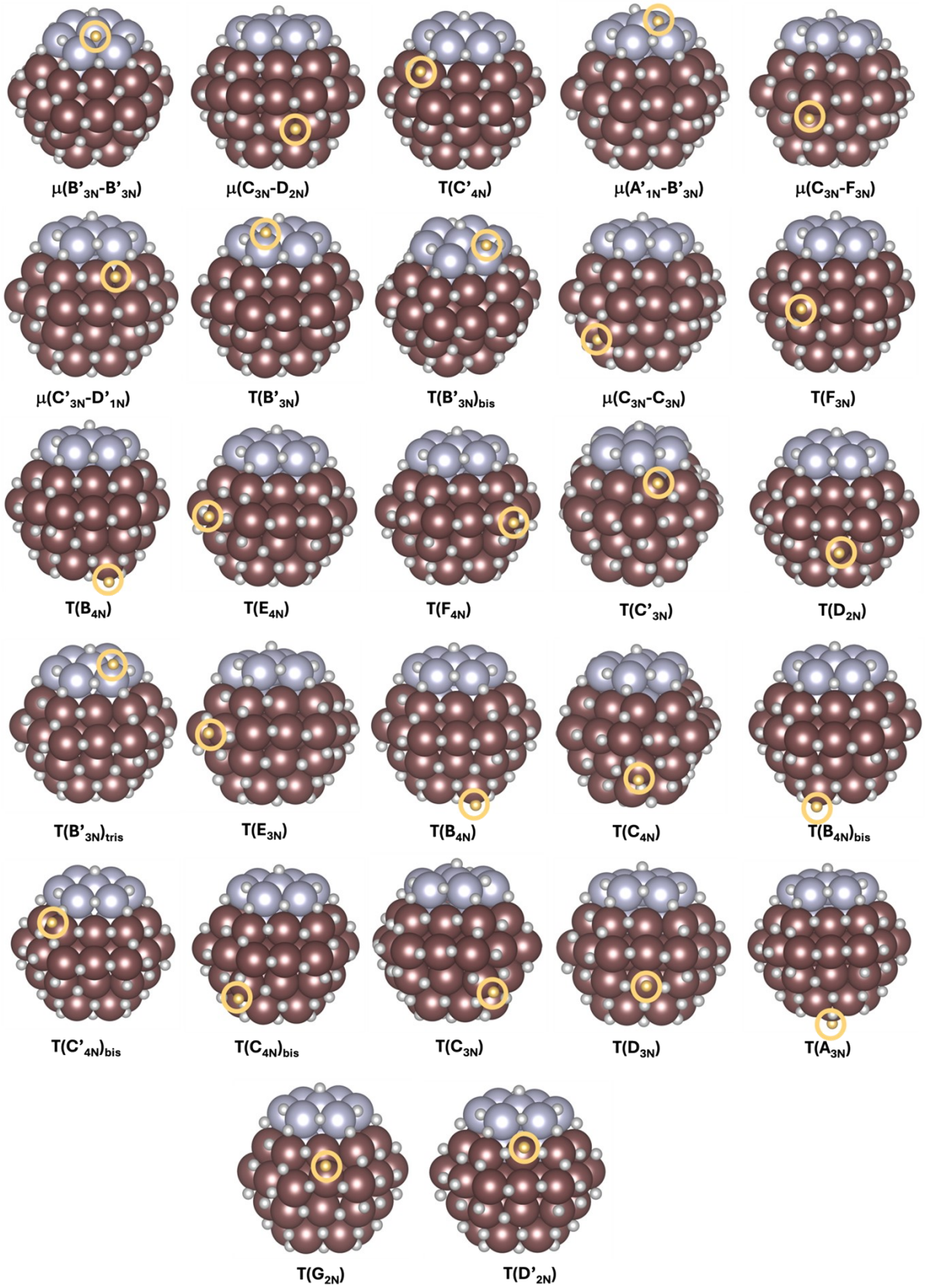

Figure S24. Optimized structures of all adsorption sites considered for the addition of one H atom to $Pt_{10}Ru_{47}H_{64}$.

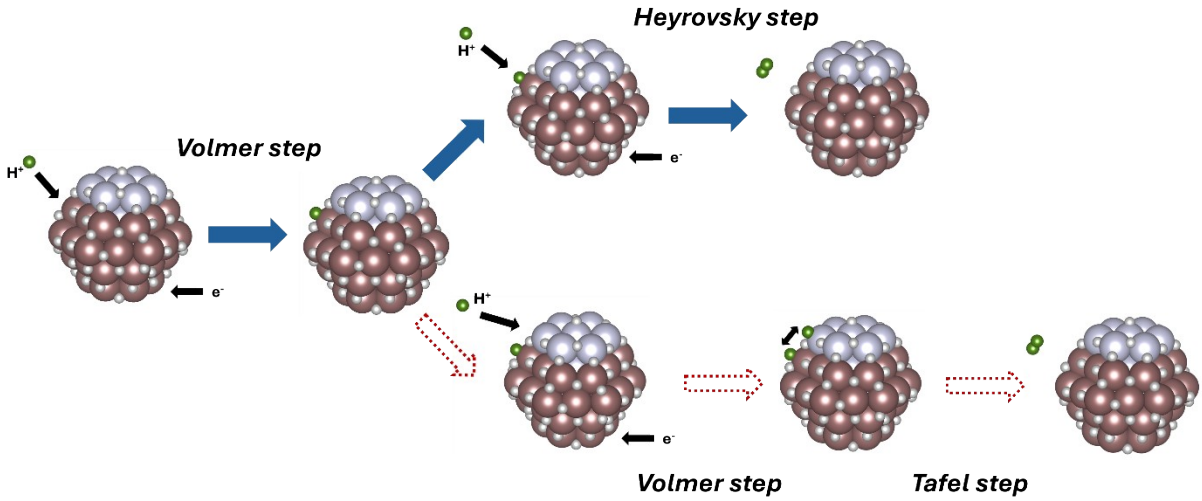

Figure S25. Hydrogen evolution reaction mechanisms taking place on the Pt-Ru interface of bimetallic nanoparticles.

Table S1. Computed adsorption energies in kJ mol^{-1} of additional H atoms on the $Pt_{79}H_{105}$, $Ru_{57}H_{61}$ and $Pt_{10}Ru_{47}H_{64}$ nanoparticles.

$Pt_{79}H_{105}$		$Ru_{57}H_{61}$		$Pt_{10}Ru_{47}H_{64}$	
Site	E_{ads}	Site	E_{ads}	Site	E_{ads}
Hollow	-50.1	$\mu(E_{3N}\text{-}F_{3N})$	-46.7	$\mu(B'_{3N}\text{-}B'_{3N})$	-45.7
$T(C_{1N})$	-35.0	$\mu(C_{3N}\text{-}D_{2N})$	-44.6	$\mu(C_{3N}\text{-}D_{2N})$	-38.2
$\mu(A_{3Y}\text{-}C_{2N})$	-34.4	$\mu(C_{3N}\text{-}D_{2N})_{bis}$	-44.5	$T(C'_{4N})$	-37.4
$T(B_{2N})$	-32.8	$\mu(C_{3N}\text{-}D_{2N})_{tris}$	-43.0	$\mu(A'_{1Y}\text{-}B'_{3N})$	-36.8
$T(B_{2N})_{bis}$	-30.1	$\mu(C_{3N}\text{-}C_{3N})$	-42.3	$\mu(C_{3N}\text{-}F_{3N})$	-34.2
$\mu(A_{4Y}\text{-}C_{1N})$	-26.8	$\mu(F_{3N}\text{-}G_{3N})$	-39.6	$\mu(C'_{3N}\text{-}D'_{1N})$	-29.0
$\mu(A_{3Y}\text{-}B_{2Y})$	-26.1	$\mu(C_{3N}\text{-}D_{1N})$	-30.6	$T(B'_{3N})$	-28.2
$T(A_{3N})$	-20.4	$T(F_{4N})$	-26.7	$T(B'_{3N})_{bis}$	-25.2
$T(C_{3N})$	-16.6	$T(F_{4N})_{bis}$	-24.6	$\mu(C_{3N}\text{-}C_{3N})$	-24.6
$T(C_{3N})_{bis}$	-10.4	$T(B_{4N})$	-24.1	$T(F_{3N})$	-21.5
$T(A_{4Y})$	-2.7	$T(C_{4N})$	-22.9	$T(B_{4N})$	-20.5
$T(A_{4Y})$	-2.1	$T(F_{3N})$	-17.4	$\mu(C_{3N}\text{-}C_{3N})$	-19.6
$T(A_{5Y})_{bis}$	+8.0	$T(B_{4N})_{bis}$	-14.7	$T(E_{4N})$	-19.5
$T(C_{2Y})^a$	+10.7	$T(E_{3N})$	-11.3	$T(F_{4N})$	-17.4
$T(B_{3Y})^a$	+14.7	$T(C_{4N})_{bis}$	-9.7	$T(C'_{3N})$	-15.8
		$T(D_{1N})$	-8.1	$T(D_{2N})$	-15.4
		$T(G_{2N})$	-4.0	$T(B'_{3N})tris$	-15.2
		$T(C_{3N})$	+3.7	$T(E_{3N})$	-14.8
		$T(A_{3N})$	+6.8	$T(B_{4N})_{bis}$	-14.5
				$T(C_{4N})$	-12.0
				$T(B_{4N})$	-11.6
				$T(C'_{4N})_{bis}$	-9.3
				$T(C_{4N})_{bis}$	-5.5
				$T(C_{3N})$	-4.3
				$T(D_{3N})$	+2.4

	$T(A_{3N})$	+3.5
	$T(G_{2N})$	+6.0
	$T(D'_{2N})$	+13.4

[a] H_2 is formed during optimization

Table S2. Mean computed adsorption energies (kJ mol^{-1}) of the H monolayer formation ($Ru_{57}H_{44}$ and $Pt_{79}H_{60}$) as well as the mean adsorption energy of the subsequent additional H atoms.

$Ru_{57}H_x$	E_{ads}	$Pt_{79}H_x$	E_{ads}
43	-65.7	60	-55.8
55	-49.9	75	-41.8
61	-50.1	90	-36.5
66	-30.6	105	-29.1
77	-21.8	120	-26.0

Table S3. Comparison of the most relevant graphene-derived and Pt and/or Ru graphene-based HER nanoelectrocatalysts under acidic conditions. Parameters: mean diameter (Ø), onset overpotential (η_0, mV), overpotential at |j| =10 mA/cm^2 (η_{10}, mV), Tafel slope (b, mV/dec), and exchange current density ($|j_0|$, mA/cm^2). Unless otherwise stated, electrolyte is 0.5 M H_2SO_4.

Entry	catalyst	Ø(nm)	η_0 (mV)	η_{10} (mV)	b (mV/dec)	$\|j_0\|$(mA/cm^2)	Ref.
1 [a]	Ru_5Pt_1@NH_2-rGO activated	1.7	≈0	3	46	0.944	This work
2 [a]	Ru@NH_2-rGO activated	1.6	≈0	20	36	2.860	This work
3 [a]	Ru-r@P-rGO	1.4	≈0	2	51	10.88	1
4	$Pt_{0.47}$-Ru/Acet	1.46	-	28	33.3	-	2
5	Ru/D-NPC	5.4	-	68	41.7	2.51	3
6	PtRu@RFCS-6h	2.57	2.3	19.7	27.2	1.57	4
7	$Pd_3Pt_{29}Ru_{62}Te_6$	5	-	39	32	0.45	5
8	Ru@C_2N	1.6±0.5	9.5	22	30	1.9	6
9	Ru-HMT-MP-7	9.5	-	29	19.3	-	7
10	Ru/(B-N)-PC	2~3	-	15	22.6	-	8
11	Pt_1Ru_1/NMHCS-A	-	-	22	38	-	9
12	3-GRR Pt−WC/CNT	-	-	25	22.3	-	10
13	Pt/CoO_x-HCS-3000	2~4	-	28	31	-	11
14	Ru@β-HATB/CC	2.35	-	25	27.6	1.305	12
15	Ru_2P/RGO-20	7		22	29	2.2	13
16	Ru/GLC	2~5	3	35	46	-	14
17	$PtRu_2$/PF	2~3	10	22	30	2.81	15
18	PtRu/CC_{1500}	<3	-	8	25	2.44	16
19	Pt53Ru39Ni8	55	-(looks like 0)	37	34	-	17
20	RuP2@NPC	8	≈0	38	38	1.99	18
21 [a]	Ru@rGO-r	2.6	-	29	48	2.50	19
22 [a]	Ru@P-rGO-r	3.3	-	15	49	4.97	19
23	Ru_1Pt_2@rGO	3.0	-	6	20.9	-	20

[a] 1M H_2SO_4

Abbreviations used on Table S3:

P-rGO: phosphorous dopped reduced graphene oxide

Acet: commercial acetylene black

D-NPC: defect-rich nitrogen and phosphorus co-doped carbon nanosheets

RFCS: resorcinol– formaldehyde (RF) carbon spheres

C_2N: nitrogenated holey two-dimensional carbon structure

Ru-HMT-MP-7: RuO2-RuP2/Ru on the N, P co-doped carbon matrix

(B-N)-PC: B, N co-doped polar carbon

NMHCS-A: activated N- doped mesoporous hollow carbon sphere

3-GRR Pt−WC/CNT :3-multistep galvanic replacement reaction Tungsten carbide carbon nanotubes

HCS-3000: hollow carbon sphere after 3000 cyclic voltammetry (CV) cycles

β-HATB/CC :β-hexagonal ammonium tungsten bronze/ carbon cloth

Ru2P/RGO-20: reduced graphene oxide nanosheets

GLC: graphene-like layered carbon

PF : polyethylenedioxythiophene with trace amount of Fe

CC_{1500}: carbon-cloth-supported after 1500 ECD cycles

RuP2@NPC: N,P dual-doped carbon-encapsulated ruthenium diphosphide

References

1. Mallón, L. et al. Effect of Nitrogen and Phosphorus Doping of Reduced Graphene Oxide in the Hydrogen Evolution Catalytic Activity of Supported Ru Nanoparticles, ACS Appl. Mater. Interfaces, 17, 6198–6210 (2025)
2. Chen, Y. et al. Plasma-assisted highly dispersed Pt single atoms on Ru nanoclusters electrocatalyst for pH-universal hydrogen evolution. Chem. Eng. J. 448, 137611 (2022).
3. Li, W. et al. Monodispersed ruthenium nanoparticles interfacially bonded with defective nitrogen-and-phosphorus-doped carbon nanosheets enable pH-universal hydrogen evolution reaction. Appl. Catal. B Environ. 306, 121095 (2022).
4. Li, K. et al. Enhanced electrocatalytic performance for the hydrogen evolution reaction through surface enrichment of platinum nanoclusters alloying with ruthenium: In situ embedded in carbon. Energy Environ. Sci. 11, 1232–1239 (2018).
5. Liu, S. et al. Cation vacancy-modulated PtPdRuTe five-fold twinned nanomaterial for catalyzing hydrogen evolution reaction. Nano Energy 61, 346–351 (2019).
6. Mahmood, J. et al. An efficient and pH-universal ruthenium-based catalyst for the hydrogen evolution reaction. Nat. Nanotechnol. 12, 441–446 (2017).
7. Zhao, Y. et al. Heterostructure of RuO2-RuP2/Ru Derived from HMT-based Coordination Polymers as Superior pH-Universal Electrocatalyst for Hydrogen Evolution Reaction. Small 18, 1–10 (2022).
8. Xu, S. et al. Size control and electronic manipulation of Ru catalyst over B, N co-doped carbon network for high-performance hydrogen evolution reaction. Nano Res. 16, 6212–6219 (2022).
9. Zhao, W. et al. Pt-Ru Dimer Electrocatalyst with Electron Redistribution for Hydrogen Evolution Reaction. ACS Catal. 12, 5540–5548 (2022).
10. Chu, Y. et al. Modulating Dominant Facets of Pt through Multistep Selective Anchored on WC for Enhanced Hydrogen Evolution Catalysis. ACS Appl. Mater. Interfaces 15, 9263–9272 (2023).
11. Wang, Y. et al. Hollow carbon sphere-supported Pt/CoOx hybrid with excellent hydrogen evolution activity and stability in acidic environment. Appl. Catal. B Environ. 314, (2022).
12. He, W., et al. Tuning charge distribution of Ru nanoparticles via coupling ammonium tungsten bronze as Pt-Like electrocatalyst for hydrogen evolution reaction. Chem. Eng. J. 436, 135044 (2022).
13. Liu, T. et al. Ultrasmall Ru2P nanoparticles on graphene: A highly efficient hydrogen evolution reaction electrocatalyst in both acidic and alkaline media. Chem. Commun. 54, 3343–3346 (2018).

14. Chen, Z. et al. Ruthenium/Graphene-like Layered Carbon Composite as an Efficient Hydrogen Evolution Reaction Electrocatalyst. ACS Appl. Mater. Interfaces 8, 35132–35137 (2016).
15. Pang, L. et al. Enhanced electrocatalytic activity of PtRu/nitrogen and sulphur co-doped crumbled graphene in acid and alkaline media. J. Colloid Interface Sci. 590, 154–163 (2021).
16. Li, L., et al. Electrochemical formation of PtRu bimetallic nanoparticles for highly efficient and pH-universal hydrogen evolution reaction. J. Mater. Chem. A 8, 2090–2098 (2020).
17. Shi, Y. C., et al.. Rapid fabrication of support-free trimetallic Pt53Ru39Ni8 nanosponges with enhanced electrocatalytic activity for hydrogen evolution and hydrazine oxidation reactions. J. Colloid Interface Sci. 505, 14–22 (2017).
18. Pu, Z., et al. RuP2-Based Catalysts with Platinum-like Activity and Higher Durability for the Hydrogen Evolution Reaction at All pH Values. Angew. Chemie - Int. Ed. 56, 11559–11564 (2017).
19. Mallón, L., et al. Ru nanoparticles supported on alginate-derived graphene as hybrid electrodes for the hydrogen evolution reaction, New J. Chem. 46 (2022) 49–56.
20. Yang, J. et al. Highly Dispersed Ru-Pt Heterogeneous Nanoparticles on Reduced Graphene Oxide for Efficient pH-universal Hydrogen Evolution, Adv. Funct. Mater. 34, 2411081 (2024)